

The boundary-constraint method for constructing vortex-surface fields



Shiying Xiong^a, Yue Yang^{a,b,c,*}

^a State Key Laboratory for Turbulence and Complex Systems, College of Engineering, Peking University, Beijing 100871, China

^b Center for Applied Physics and Technology, College of Engineering, Peking University, Beijing 100871, China

^c Beijing Innovation Center for Engineering Science and Advanced Technology, Peking University, Beijing 100871, China

ARTICLE INFO

Article history:

Received 10 December 2016

Received in revised form 7 February 2017

Accepted 7 March 2017

Available online 10 March 2017

Keywords:

Vortex identification

Vortex dynamics

Vortex-surface field

Boundary constraint

Shear flow

ABSTRACT

We develop a boundary-constraint method for constructing the vortex-surface field (VSF) in a three-dimensional fluid velocity–vorticity field. The isosurface of the VSF is a vortex surface consisting of vortex lines, which can be used to characterize the evolution of vortical structures in a Lagrangian sense. The evolution equation with pseudo-time is solved under the VSF boundary constraint to obtain a numerical solution of the VSF. Compared with the existing two-time method, the boundary-constraint method constructs the VSF from a single velocity dataset at a given time instead of a time series of velocity fields starting from a simple condition. This improvement significantly increases the applicability of the VSF method and reduces the demanding computational cost and required velocity data size. Using the boundary-constraint method, we construct the VSFs in Taylor–Green flow and transitional channel flow. In addition, the uniqueness of the VSF solution is discussed and the convergence of the error in the calculation of VSFs is analyzed.

© 2017 Elsevier Inc. All rights reserved.

1. Introduction

Vortices are often described as “the sinews and muscles of turbulence” [1], but their identification is hindered by the lack of consensus on the mathematical definition. The existing techniques of the vortex identification can be categorized into Eulerian- and Lagrangian-based approaches.

Eulerian-based methods of the vortex identification define a function evaluated point-by-point and then classify each point as being inside or outside a vortex using a criterion based on the point values. Based on the kinematics implied by the vorticity or the velocity gradient tensor, some Eulerian vortex-identification techniques were proposed, e.g., the Q -criterion [2], the λ_2 -criterion [3], the Δ -criterion [4], and the swirling strength [5]. These Galilean-invariant vortex criteria can effectively identify some typical vortical structures, in particular, the “vortex cores”, but they also have some weaknesses [6,7]. Since the Eulerian methods are based on the instantaneous local velocity field, they cannot characterize the interaction between the vortical structures lying at different locations [8], and characterize the continuous temporal evolution of a vortical structure [9].

Lagrangian-based methods of the vortex identification appear to be more natural to describe the continuous evolution of vortical structures than the Eulerian approach. Based on the vortex-dynamic paradigm in fluid mechanics, the vortex-surface

* Corresponding author at: 310 Building 1, College of Engineering, Peking University, Beijing 100871, China.

E-mail address: yyg@pku.edu.cn (Y. Yang).

field (VSF), which identifies vortices using the isosurfaces of the VSF, was proposed by Yang and Pullin [10]. In a general sense, the vortex surface—examples of which are vortex tubes and sheets [11,12]—can be defined as a smooth surface or manifold embedded within a three-dimensional velocity field, the property of which is that the vorticity is tangent to the surface at any point.

The VSF ϕ_v , a smooth scalar function, satisfies the constraint that the gradient of ϕ_v is normal to the vorticity everywhere. This constraint is a first-order homogeneous linear partial differential equation whose characteristic equation is a three-dimensional nonlinear dynamical system [13]. Thus the construction of vortex surfaces can be considered as a special case of finding two-dimensional invariant manifolds or invariant tori of a three-dimensional vector field. The calculation of a smooth invariant manifold for a finite-dimensional system was investigated using block M-matrix properties to establish the stability and error estimation [14,15]. The invariant tori in Hilbert space were computed by the Fourier method [16]. The Lagrangian coherent structure was constructed to capture the distinguished surface of trajectories in a dynamical system, which exerts a major influence on nearby trajectories over a time interval of interest [17–19]. The construction of vortex surfaces in highly symmetric flow was solved analytically using first integrals [20]. However, the existence of globally smooth vortex surfaces in general three-dimensional flows remains an open problem.

Besides the construction of the VSF, the evolution of the VSF is of importance in fluid dynamics. Helmholtz [21] obtained a central result in vortex dynamics: the vortex lines or surfaces move with fluids as material lines or surfaces, respectively, in a perfectly inviscid flow. On the contrary, the vortex surfaces are no longer material surfaces in a viscous flow, so we cannot simply “track” the vortex lines and surfaces in an exact Lagrangian manner in real viscous flows. From the Lagrangian view, some vortex methods based on vortical elements such as vortex particles [22], vortex filaments [23], and vortex sheets [24,25] are developed to compute vortical flows by tracking a number of vortical elements with the aid of substantial computational resources, and they require re-meshing and regularization techniques to deal with the topological change of vortical structures.

The evolution of material surfaces that are vortex surfaces at the initial time in highly symmetric viscous flows [10] and transitional channel flows [9] were investigated, and the deviation of the material surface from the vortex surface is quantified by the cosine of the angle between the vorticity and the gradient of the VSF. The results demonstrate that the deviation between the vortex surfaces and material surfaces becomes significant after the topological changes of vortical structures such as vortex reconnection.

The two-time method is developed to characterize the evolution of vortex surfaces in viscous flows properly [26]. This Lagrangian-based method provides a numerical dissipative regularization for the ill-posed governing equations of the VSF in viscous flows for studying vortex deformation and reconnection [27]. In particular, the two-time method has been applied to Taylor–Green (TG) flow, Kida–Pelz flow, and the transitional channel flow to display the temporal evolution of vortex surfaces. Numerical results on the evolution of VSFs clarify the continuous vortex dynamics in these transitional flows including vortex reconnection, rolling-up of vortex tubes, vorticity intensification between anti-parallel vortex tubes, and vortex stretching and twisting from a Lagrangian perspective. This suggests a possible scenario for explaining the transition from a smooth laminar flow to turbulent flow and scale cascade in terms of topology and geometry of vortex surfaces.

In the vortex identification, the VSF uses evolving vortex surfaces along with attached vortex lines and their vorticity magnitude to characterize vortical structures. Thus the VSF combines the strengths of the passive scalar for showing the Lagrangian-based vortex evolution and the Eulerian vortex criteria for identifying the strong vortical elements. At the meantime, the VSF overcomes the weaknesses of the existing methods. It builds an explicit mapping from a scalar field to a vorticity field and displays the whole vortical structure as a vortex surface rather than broken vortex cores. In addition, the VSF can effectively identify the vortex reconnection [28] that is a critical process for the scale cascade in transitions and is hard to be characterized via Eulerian-based methods in shear flows [29]. On the other hand, the implementation of the two-time method requires a temporally-resolved series of velocity fields [26,29], which can be demanding for high-Reynolds-number turbulent flows, and requires an accurate initial VSF solution, which in general only exists in the flows with vanishing helicity density [20].

In the present study, we develop a new boundary-constraint method for constructing VSFs, which can overcome the weaknesses of the two-time method. The evolution equation with pseudo-time is solved under the boundary constraint of the VSF to obtain an approximate VSF solution. Compared with the two-time method, the boundary-constraint method can construct the VSF from a single velocity dataset instead of the time series, so the computational cost can be significantly reduced. In the development of the boundary-constraint method, several important issues are addressed, including the requirement for the vorticity field, the convergence of the error, and the uniqueness of the VSF solution.

The outline of this paper is as follows. In section 2, we review the VSF and the two-time method, and then we propose the boundary-constraint method. In section 3, we present the numerical method for solving the boundary-constraint equations and analyze the convergence of the error in the calculation of the VSF. In section 4, the evolution of VSFs in two typical transitional flows, i.e., TG flow and transitional channel flow, is calculated. Additionally, the uniqueness of the VSF solution obtained from the boundary-constraint method and the two-time method is discussed. Some conclusions are drawn in section 5.

2. Methods for constructing the VSF

2.1. Constraint of the VSF

The VSF $\phi_v(\mathbf{x}, t)$ is defined as a globally smooth scalar field whose isosurface is the vortex surface consisting of vortex lines, where \mathbf{x} is the coordinates in three-dimensional space and t is physical time. The corresponding constraint for the VSF [10] is

$$\mathcal{C}_v \equiv \boldsymbol{\omega} \cdot \nabla \phi_v = 0, \quad (1)$$

where $\boldsymbol{\omega}(\mathbf{x}, t) = (\omega_x, \omega_y, \omega_z) \equiv \nabla \times \mathbf{u}$ is the vorticity calculated from the velocity field $\mathbf{u}(\mathbf{x}, t) = (u_x, u_y, u_z)$. Eq. (1) is a first-order linear homogeneous partial differential equation, and its characteristic equation is

$$\frac{dx}{\omega_x(\mathbf{x}, t)} = \frac{dy}{\omega_y(\mathbf{x}, t)} = \frac{dz}{\omega_z(\mathbf{x}, t)}. \quad (2)$$

Setting

$$\frac{dx}{\omega_x} = \frac{dy}{\omega_y} = \frac{dz}{\omega_z} = ds \quad (3)$$

in Eq. (2) with the arclength s yields a nonlinear autonomous system [30]

$$\frac{d\mathbf{x}}{ds} = \boldsymbol{\omega}(\mathbf{x}, t). \quad (4)$$

From the theory of the ordinary differential equation (ODE) [13], it is necessary and sufficient that any solution ϕ_v of Eq. (1) is a first integral of Eq. (4), and Eq. (4) can have multiple independent first integrals.

The general, globally smooth solution of Eq. (1), namely the VSF in the context of vortex dynamics, can be expressed as $\phi_v = F(\Phi_1, \Phi_2)$, where Φ_1 and Φ_2 are two independent first integrals of Eq. (4). The continuously differentiable function F should be carefully selected to remove the possible singularities in Φ_1 and Φ_2 . The non-unique F implies that Eq. (1) admits multiple independent solutions for ϕ_v [10,20]. This non-uniqueness issue can be partly resolved by the additional constraint on ϕ_v [9] or the numerical method with appropriate regularization as discussed in section 4.4.

In the flows with the vanishing helicity density $h \equiv \mathbf{u} \cdot \boldsymbol{\omega} = 0$, the first integrals of Eqs. (4) can be constructed analytically [20]. Nonetheless, for a general vorticity field with $h \neq 0$, Eq. (4) may not be integrable. In other words, the exact VSF solution under the constraint Eq. (1) may not exist, so we have to seek an approximate solution of Eq. (1) using numerical methods.

2.2. The two-time method

The two-time method can be applied to both incompressible and compressible flows, but here we only consider the former one. In a three-dimensional incompressible viscous flow, the velocity field is governed by the Navier–Stokes (NS) equations

$$\begin{cases} \frac{\partial \mathbf{u}}{\partial t} + (\mathbf{u} \cdot \nabla) \mathbf{u} = -\frac{1}{\rho} \nabla p + \nu \nabla^2 \mathbf{u}, \\ \nabla \cdot \mathbf{u} = 0, \end{cases} \quad (5)$$

with proper initial and boundary conditions, where p denotes the pressure, ρ the density, and ν the kinematic viscosity.

Given the time-resolved velocity fields obtained from the NS equations, the evolution of the VSF can be calculated using the two-time method [26]. Firstly, an initial VSF $\phi_{v0} \equiv \phi_v(\mathbf{x}, t = 0)$ is constructed to satisfy the initial VSF constraint

$$\boldsymbol{\omega}_0 \cdot \nabla \phi_{v0} = 0, \quad (6)$$

where $\boldsymbol{\omega}_0 \equiv \boldsymbol{\omega}(\mathbf{x}, t = 0)$ is the initial vorticity field. Secondly, each time step is divided into prediction and correction steps. In the prediction step, the temporary VSF ϕ_v^* is computed as

$$\frac{\partial \phi_v^*(\mathbf{x}, t)}{\partial t} + \mathbf{u}(\mathbf{x}, t) \cdot \nabla \phi_v^*(\mathbf{x}, t) = \epsilon \nabla^2 \phi_v^*, \quad t > 0 \quad (7)$$

with well-defined boundary conditions, where ϵ is a small effective diffusivity for numerical regulation, which can be given explicitly for the diffusion term or determined implicitly by a diffusive numerical scheme for the convection term. In general, the temporary ϕ_v^* deviates from an accurate VSF owing to the breakdown of the Helmholtz vorticity theorem in viscous flows, so ϕ_v^* is projected onto the desired VSF solution through the correction step. In the correction step, ϕ_v^* is evolved in pseudo-time τ at a fixed physical time t as

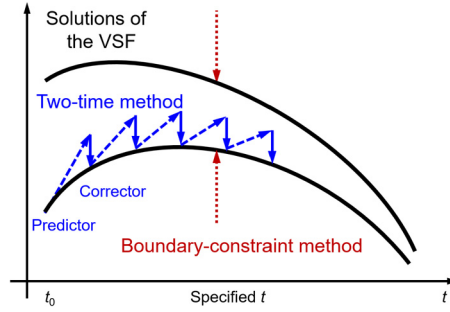


Fig. 1. Sketch of the numerical implementation of the two methods for computing the VSF (solid curve: solution of the VSF; dashed arrow: prediction step in the two-time method; solid arrow: correction step in the two-time method; dotted arrow: the boundary-constraint method).

$$\frac{\partial \phi_v(\mathbf{x}, t; \tau)}{\partial \tau} + \boldsymbol{\omega}(\mathbf{x}, t) \cdot \nabla \phi_v(\mathbf{x}, t; \tau) = \epsilon \nabla^2 \phi_v, \quad 0 < \tau \leq T_\tau \quad (8)$$

with the initial condition $\phi_v(\mathbf{x}, t; \tau = 0) = \phi_v^*(\mathbf{x}, t)$ and well-defined boundary conditions, where T_τ is a pseudo-time period that is typically less than 100 times of the size of the physical time step. Finally, $\phi_v^*(\mathbf{x}, t)$ in Eq. (7) is updated by $\phi_v(\mathbf{x}, t; \tau = T_\tau)$ from Eq. (8) for each physical time step. This predictor–corrector procedure is sketched as dashed and solid arrows in Fig. 1. The numerical schemes for solving Eqs. (7) and (8) are described in detail in [26].

2.3. The boundary-constraint method

Although the two-time method has been successfully used for characterizing the evolution of VSFs and analyzing Lagrangian vortex dynamics in highly symmetric flows [26] and transitional channel flows [29], there are two major weaknesses of the two-time method, one is the initial velocity–vorticity field must be simple enough to ensure that Eq. (6) can be solved, the other is that the computation may need very large dataset for time-resolved velocity fields. Therefore, we develop the boundary-constraint method to overcome these weaknesses.

The boundary-constraint equation is proposed as

$$\begin{cases} \frac{\partial \phi_v}{\partial \tau} + \boldsymbol{\omega} \cdot \nabla \phi_v = \epsilon \nabla^2 \phi_v, & \mathbf{x} \in \Omega, \quad 0 < \tau \leq T_\tau, & \text{(a)} \\ \boldsymbol{\omega} \cdot \nabla \phi_v = 0, & \mathbf{x} \in \partial\Omega, \quad 0 < \tau \leq T_\tau, & \text{(b)} \\ \phi_v = \phi_{v0}, & \mathbf{x} \in \Omega, \quad \tau = 0, & \text{(c)} \end{cases} \quad (9)$$

where Ω denotes the computational domain. As used in Eqs. (7) and (8), the small effective diffusivity ϵ can be an explicit diffusivity or symbolically reflect the diffusivity of the numerical scheme for numerical regularization. The initial condition ϕ_{v0} should be compatible with the boundary condition. We presume that the VSF limit of $\phi_v(\mathbf{x}, t; \tau)$ exists as

$$\phi_v(\mathbf{x}, t) = \lim_{\tau \rightarrow +\infty} \phi_v(\mathbf{x}, t; \tau). \quad (10)$$

In order to demonstrate that Eq. (10) can be obtained through the boundary-constraint method, we take $\boldsymbol{\omega} \cdot \nabla$ on Eqs. (9a) and (9c) and set $\epsilon = 0$, then we obtain the pseudo-time evolution equation for C_v as

$$\begin{cases} \frac{\mathcal{D}C_v}{\mathcal{D}\tau} = 0, & \mathbf{x} \in \Omega, \quad 0 < \tau \leq T_\tau, & \text{(a)} \\ C_v = 0, & \mathbf{x} \in \partial\Omega, \quad 0 < \tau \leq T_\tau, & \text{(b)} \\ C_v = C_0, & \mathbf{x} \in \Omega, \quad \tau = 0, & \text{(c)} \end{cases} \quad (11)$$

where $C_0 = \boldsymbol{\omega} \cdot \nabla \phi_{v0}$ and

$$\frac{\mathcal{D}}{\mathcal{D}\tau} = \frac{\partial}{\partial \tau} + \boldsymbol{\omega} \cdot \nabla \quad (12)$$

is a pseudo-material-like derivative [26]. Since C_v in Eq. (11a) is a pseudo-Lagrangian field that is a constant along a vortex line owing to the frozen property, the vanishing C_v at $\partial\Omega$ can be transported into the entire Ω if all the vortex lines started from the boundary are ergodic within Ω . Hence, the limit of C_v is converged to zero everywhere as $\tau \rightarrow \infty$, and Eq. (10) can be satisfied using the boundary-constraint method. The comparison of the two-time method and the boundary-constraint method for computing VSFs is sketched in Fig. 1.

Since the solution of Eq. (11a) with $\epsilon = 0$ can develop exponentially small structures due to the straining nature of the vorticity vector field, the inclusion of a finite ϵ in Eq. (11a) is necessary to resolve a smooth VSF solution with a finite

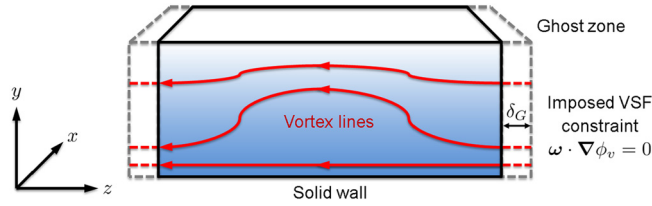


Fig. 2. Schematic diagram of the boundary-constraint method for constructing the VSF in a wall-bounded flow.

spatial resolution [26]. In the implementation, the right hand side (RHS) of Eq. (9a) is not strictly equal to zero, and the numerical diffusivity can be introduced by an upwind-type scheme for convection terms.

The diffusion term $\epsilon \nabla^2 \phi_v$ with a small effective diffusivity $\epsilon > 0$ is considered in Eq. (9a), and subsequently the pseudo-time evolution equation for C_v becomes

$$\frac{\mathcal{D}C_v}{\mathcal{D}\tau} = \epsilon \nabla^2 C_v - \epsilon \left[(\nabla^2 \boldsymbol{\omega}) \cdot (\nabla \phi_v) + 2(\nabla \boldsymbol{\omega}) \otimes (\nabla \nabla \phi_v) \right], \quad \mathbf{x} \in \Omega, \quad 0 < \tau \leq T_\tau. \quad (13)$$

The first term in the RHS in Eq. (13) serves as an artificial diffusion term, which helps to transport $C_v = 0$ at the boundary into the interior domain. The other terms in the RHS are coupled with ϕ_v and the frozen $\boldsymbol{\omega}$, and their effects on the evolution of C_v can be complicated. Thus numerical experiments are carried out in section 4 to demonstrate the effect of the artificial diffusion mechanism.

3. Numerical methods

3.1. Numerical schemes and boundary conditions

For solving Eq. (9a), ϕ_v is advanced in τ using the third-order total-variation-diminishing Runge–Kutta method, and the convection term is approximated by the fifth-order weighted essentially non-oscillatory (WENO) scheme [31]. The pseudo-time step $\Delta\tau$ should be small enough to ensure that the Courant–Friedrichs–Lewy (CFL) number

$$CFL_\omega = \Delta\tau \max \left(\frac{|\omega_x|}{\Delta x}, \frac{|\omega_y|}{\Delta y}, \frac{|\omega_z|}{\Delta z} \right), \quad (14)$$

of Eq. (9a) is less than 0.5 for the numerical stability, where Δx , Δy and Δz are grid sizes in three directions.

In the boundary-constraint method, the boundary condition of Eq. (9b) should be treated carefully. For the non-slip condition, all the vortex lines are tangent to the solid-wall boundary [32], so ϕ_v remains the initial value at the wall and it cannot be convected into the computational domain. The Dirichlet boundary condition

$$\phi_v = C_w, \quad \mathbf{x} \in \partial\Omega, \quad 0 < \tau \leq T_\tau, \quad (15)$$

is applied with a constant C_w to ensure that the planar vortex surface is attached to the solid wall.

If the boundary is not a solid wall, the vorticity direction can be arbitrary at the boundary. This boundary condition is hard to implement numerically, so we transform this boundary into the Neumann boundary condition. As shown in Fig. 2, we construct the ghost zones to stretch the vortex lines so that they are normal to the outer boundary of the ghost zone. With this technique, Eq. (9b) is degenerated into the Neumann boundary condition

$$\frac{\partial \phi_v}{\partial n} = 0, \quad \mathbf{x} \in \partial\Omega_G \quad 0 < \tau \leq T_\tau, \quad (16)$$

at the boundary $\partial\Omega_G$ of the ghost zone, where $\partial/\partial n$ denotes the partial derivative of the direction normal to the boundary.

Fig. 3 is a sketch of a two-dimensional grid for the ghost zone. Without loss of generality, we only illustrate the ghost zone for the right boundary in Fig. 2. The numerical scheme of this boundary condition is simplified as

$$\phi_v(N_z + n_G) = \phi_v(N_z + n_G - 1), \quad (17)$$

where N_z and n_G are the numbers of grids in the z -direction for the original computational domain and the ghost zone, respectively, and δ_G is the width of the ghost zone.

Next we describe how to construct the vorticity in the ghost zone. First, the temporary vorticity $\boldsymbol{\omega}^*$ in the ghost zone is obtained by the third-order spline interpolation [33,34] from original grid points (i, j, k) , where $1 \leq i \leq N_x$, $1 \leq j \leq N_y$, and $1 \leq k \leq N_z$. Then $\boldsymbol{\omega}^*$ is decomposed into two parts as

$$\boldsymbol{\omega}^* = \boldsymbol{\omega}_{//}^* + \boldsymbol{\omega}_\perp^*, \quad (18)$$

where $\boldsymbol{\omega}_{//}^*$ and $\boldsymbol{\omega}_\perp^*$ are parallel to and perpendicular to the boundary, respectively. The parallel part goes to zero smoothly within the ghost zone as

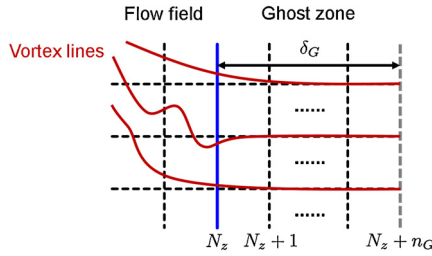


Fig. 3. Sketch of the boundary treatment and grids of the ghost zone on the y - z plane.

$$\omega_{//}(x_G) = \omega_{//}^*(x_G) f(x_G), \quad x_G \in [0, \delta_G], \tag{19}$$

with the smooth function

$$f(x_G) = \exp[-i_G (1 - \delta_G + x_G)^{i_G}], \quad x_G \in [0, \delta_G], \tag{20}$$

where x_G is the distance from the original boundary in the ghost zone and i_G is an integer. The constants $\delta_G = 0.1$ and $i_G = 100$ are selected to ensure that the transition in $f(x_G)$ is smooth in the ghost zone with a small number of grids. Finally, the vorticity in the ghost zone is stretched as

$$\omega = \omega_{//} + \omega_{\perp}^*. \tag{21}$$

We remark that the auxiliary ghost zone can improve the accuracy of the numerical scheme at the boundary, and Eq. (20) has no influence on the vorticity in the original flow field.

3.2. Deviation analysis

Eq. (9a) with the VSF boundary constraint is computed in a finite pseudo-time to obtain an approximate VSF solution. The deviation of the approximate VSF solution ϕ_v from an exact VSF is defined as the cosine of the angle between ω and $\nabla\phi_v$ as [10,35]

$$\lambda_\omega \equiv \frac{\omega \cdot \nabla\phi_v}{|\omega| |\nabla\phi_v|}. \tag{22}$$

The VSF constraint Eq. (1) implies that the exact VSF has pointwise $\lambda_\omega = 0$ within the domain of interest.

Using Eq. (9a) at fixed t and following the analysis [26], we obtain the pseudo-time evolution equation for λ_ω as

$$\frac{\mathcal{D}\lambda_\omega}{\mathcal{D}\tau} = \mathcal{A}\lambda_\omega + \mathcal{B}, \tag{23}$$

with

$$\mathcal{A}(\mathbf{x}, t; \tau) = \mathbf{n}_v \cdot \mathbf{S}_\omega \cdot \mathbf{n}_v - \mathbf{n}_\omega \cdot \nabla|\omega| - \epsilon \mathbf{R}_\Phi \mathbf{n}_v \cdot \mathbf{n}_\Phi, \tag{24}$$

and

$$\mathcal{B}(\mathbf{x}, t; \tau) = \epsilon \mathbf{R}_\Phi \mathbf{n}_\omega \cdot \mathbf{n}_\Phi, \tag{25}$$

where the entries of the symmetric part of the vorticity-gradient tensor \mathbf{S}_ω are $S_{\omega,ij} = 1/2(\partial\omega_i/\partial x_j + \partial\omega_j/\partial x_i)$, and unit vectors and a dimensionless ratio are respectively

$$\mathbf{n}_\omega = \frac{\omega}{|\omega|}, \quad \mathbf{n}_v = \frac{\nabla\phi_v}{|\nabla\phi_v|}, \quad \mathbf{n}_\Phi = \frac{\nabla^2\nabla\phi_v}{|\nabla^2\nabla\phi_v|}, \quad \mathbf{R}_\Phi = \frac{|\nabla^2\nabla\phi_v|}{|\nabla\phi_v|}. \tag{26}$$

The solution of Eq. (23) has the form of

$$\lambda_\omega = \lambda_{\omega 0} \exp\left(\int \mathcal{A} d\tau\right) + \exp\left(\int \mathcal{A} d\tau\right) \int \exp\left(-\int \mathcal{A} d\tau\right) \mathcal{B} d\tau, \tag{27}$$

where the integration path is along the characteristic line of Eq. (23), and the initial deviation is $\lambda_{\omega 0} \equiv \lambda_\omega(\mathbf{x}_0, t; \tau = 0)$ where \mathbf{x}_0 is the initial location.

The first term \mathcal{A} in the RHS of Eq. (27) is statistically negative [10] in a flow with straining motion, which implies a preferred exponential decay of λ_ω , but the decaying rate can be slow in the two-time method [26]. Because as implied by Eq. (11a), \mathcal{C}_v , the numerator of Eq. (27), generally remains constant in the corrector of the two-time method without the VSF boundary constraint Eq. (11b), e.g., in isotropic box turbulence with periodic boundary conditions [27]. In this circumstance,

the decay of λ_ω is only attributed from the increase of $|\nabla\phi_v|$ in the dominator, and $\max(|\phi_v|) \sim O(1/\Delta x)$ is bounded due to the finite spatial resolution.

In the boundary-constraint method, if \mathbf{x}_0 is at the boundary with $\lambda_{\omega 0} = 0$, Eq. (27) becomes

$$\lambda_\omega(\mathbf{x}, t; \tau) = \exp\left(\int \mathcal{A}(\mathbf{x}, t; \tau) d\tau\right) \int \exp\left(-\int \mathcal{A}(\mathbf{x}, t; \tau) d\tau\right) \mathcal{B}(\mathbf{x}, t; \tau) d\tau \tag{28}$$

along the characteristic line of Eq. (23) from the boundary point \mathbf{x}_0 to an interior point \mathbf{x} . As discussed in section 2.3, if the entire computational domain is filled with the vortex lines started from the boundary, then Eq. (28) can be valid for every point in the computational domain for large pseudo-times, which represents the small deviation introduced by the necessary numerical diffusion for regularization.

Since the characteristic vorticity scale of Eq. (23) is $\langle|\omega|\rangle$, where $\langle\cdot\rangle$ denotes the volume average, the characteristic pseudo-time scale for the deviation decay is

$$T_v = \frac{L_\Omega}{\langle|\omega|\rangle}, \tag{29}$$

where L_Ω is the characteristic length scale of the computational domain. For example, L_Ω is the diagonal length of Ω for a cuboid Ω . This pseudo-time scale is used to scale the required total pseudo-time period T_τ in section 4.3.

The length of the integration path of Eq. (28) is finite owing to the bounded computational domain. This implies that

$$\lim_{\tau \rightarrow \infty} |\lambda_\omega| = 0 \tag{30}$$

as $\epsilon = 0$ in Eq. (9a) and $\mathcal{B} = 0$ in Eq. (28). For a finite ϵ in the numerical implementation, we found the limit is

$$\lim_{\tau \rightarrow \infty} \langle|\lambda_\omega|\rangle \sim f_w(\epsilon), \tag{31}$$

from numerical experiments, where f_w is a nonlinear function that is discussed in section 4.3.

4. Construction and evolution of VSFs

In previous studies, the VSF has been applied to the TG flow [26] and the transitional channel flow [29] for investigating the vortex dynamics in the transition using the two-time method. In this section, we revisit the evolution of VSFs in these two flow cases using the boundary-constraint method. The objectives are twofold: (1) validate that if the boundary-constraint method can reproduce the major results from the two-time method with much less computational cost and velocity data requirement; (2) discuss the uniqueness of the VSF solutions calculated from different methods and initial conditions.

4.1. TG flow

The DNS of the TG flow is carried out to obtain the Eulerian flow field [10,26]. The initial velocity field of the TG flow [36,37] is

$$\mathbf{u} = (u_x, u_y, u_z) = (\sin x \cos y \cos z, -\cos x \sin y \cos z, 0). \tag{32}$$

The NS equation (5) in a periodic box of side 2π with the initial condition Eq. (32) is computed using the pseudo-spectral method on uniform grids $N_x \times N_y \times N_z = 512 \times 512 \times 512$ for the Reynolds number $Re = 1/\nu$.

For calculating the evolution of VSFs in TG flows, the TG symmetries [37] are utilized to reduce the computational cost. The computational domain of Eq. (9a) for TG flows is selected as

$$\mathbf{x} \in [0, \pi/2] \times [0, \pi/2] \times [\pi/2, \pi]. \tag{33}$$

The vorticity is perpendicular to the boundary of $z = \pi$, namely $\omega_x|_{z=\pi} = \omega_y|_{z=\pi} = 0$, so the Neumann boundary condition

$$\left. \frac{\partial \phi_v(\mathbf{x}, t; \tau)}{\partial z} \right|_{z=\pi} = 0 \tag{34}$$

is applied. The other boundary conditions are constructed using the TG symmetry.

Two independent initial conditions

$$\begin{cases} \phi_{v0}^{(1)} = \frac{1}{2}(\cos 2x - \cos 2y) \cos z, & \text{(a)} \\ \phi_{v0}^{(2)} = \cos x \cos y \cos z & \text{(b)} \end{cases} \tag{35}$$

are constructed using independent first integrals [20]. The isosurfaces of $\phi_{v0}^{(1)}$ and $\phi_{v0}^{(2)}$ within the periodic domain $0 \leq x, y, z \leq 2\pi$ are shown in Fig. 4.

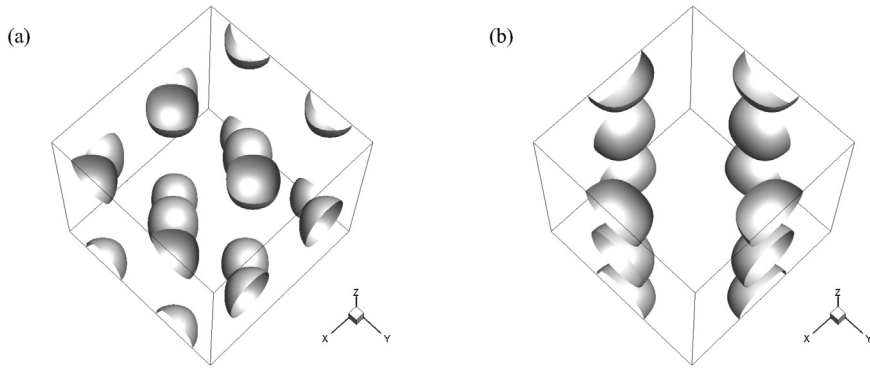


Fig. 4. Isosurfaces of initial conditions in TG flow. Scalar value is extracted as $\phi_{v0} = 0.5$. (a) $\phi_{v0}^{(1)} = \frac{1}{2}(\cos 2x - \cos 2y) \cos z$, (b) $\phi_{v0}^{(2)} = \cos x \cos y \cos z$.

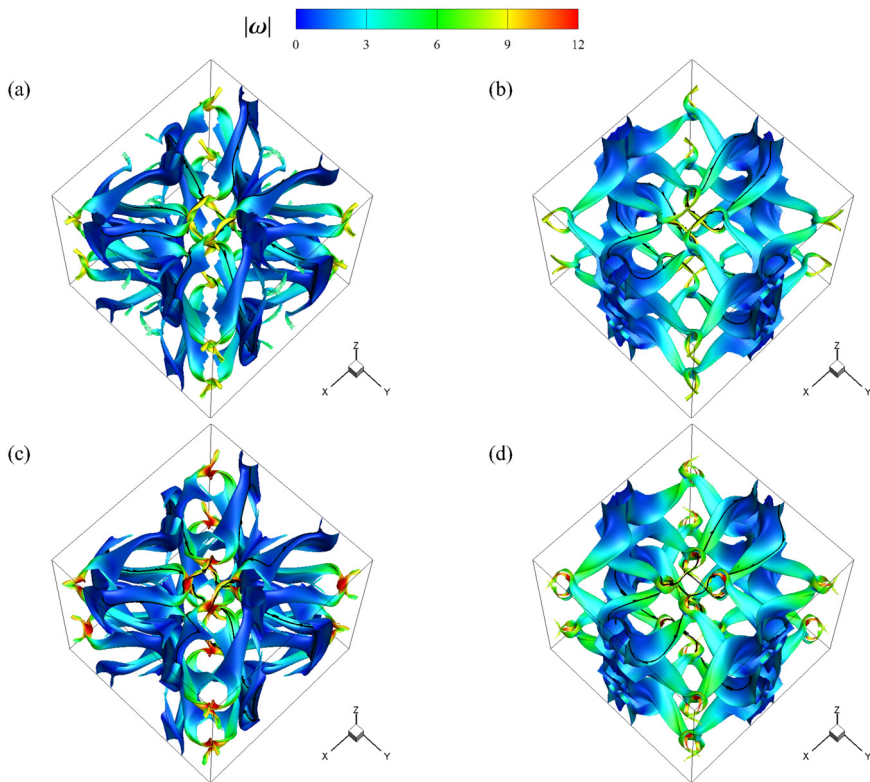


Fig. 5. Isosurfaces of the VSF in TG flows from two independent initial conditions for different Reynolds numbers at $t = 6$. The color on the surfaces is rendered by $0 \leq |\omega| \leq 12$. Some vortex lines are integrated and plotted on the isosurfaces of $\phi_v = 0.9$. (a) $Re = 400$, $\phi_{v0} = \phi_{v0}^{(1)}$, (b) $Re = 400$, $\phi_{v0} = \phi_{v0}^{(2)}$, (c) $Re = 800$, $\phi_{v0} = \phi_{v0}^{(1)}$, (d) $Re = 800$, $\phi_{v0} = \phi_{v0}^{(2)}$. (For interpretation of the colors in this figure, the reader is referred to the web version of this article.)

The evolution of VSFs is calculated on the uniform grids $N_x \times N_y \times N_z = 129 \times 129 \times 129$. The isosurfaces of the VSFs at $Re = 400$ and $Re = 800$ with different initial conditions $\phi_{v0} = \phi_{v0}^{(1)}$ and $\phi_{v0} = \phi_{v0}^{(2)}$ are compared at $t = 6$ in Fig. 5. The color on the isosurfaces of ϕ_v is rendered by $0 \leq |\omega| \leq 12$ from blue to red. Some vortex lines are integrated from the points on the extracted vortex surfaces. We can see that the vortex lines are almost on the vortex surfaces owing to the very small deviation in the simulation.

As shown in Fig. 5, the initially large-scale, blob-like vortex surfaces break down into tube-like structures, and they are twisted and flattened either by self-induced dynamics or interactions with others. In addition, the vortex surfaces at $Re = 800$ are more curved than those at $Re = 400$. The curved and twisted vortex tubes are related to the intermittent statistics in turbulence [38,39] and the continuous evolution of vortex surfaces is helpful for understanding the transition mechanism in viscous flows, which have been extensively discussed in [26].

By comparing the results with different ϕ_{v0} , we find that the statistical geometry of vortex surfaces is insensitive to their initial conditions. It implies that the boundary-constraint method appears to restore the uniqueness of the VSF solution for long times, which is discussed further in section 4.4.

4.2. Transitional channel flow

The NS Eq. (5) with forcing is solved in a channel with sides $L_x = 5.61$, $L_y = 2$ and $L_z = 2.99$ in the streamwise x -, the wall-normal y - and the spanwise z -directions, respectively. Here, the velocity \mathbf{u} is non-dimensionalized by the bulk velocity $U_b = \int_0^{2\delta} u_x dy / L_y$, where the channel half-height is set to be $\delta = 1$. A time-dependent external force $f(t)$ is added in the RHS of Eq. (5) to maintain a constant mass flux in the streamwise direction with $U_b \approx 1$.

The Fourier–Chebyshev pseudo-spectral method [40] is used to solve Eq. (5). The non-slip boundary condition is applied to the solid walls at $y = 0$ and $y = 2\delta$, and the periodic boundary condition is applied to both streamwise and spanwise directions. In order to trigger the Klebanoff-type transition, a two-dimensional and a couple of three-dimensional Tollmien–Schlichting waves are imposed on the initial laminar Poiseuille flow. The numerical solver and initial disturbances used in the DNS have been described in detail in [9,41].

The wall-friction Reynolds number $Re_\tau \equiv u_\tau \delta / \nu = 207.8$ is calculated after the flow reaches the fully developed turbulent state, where $u_\tau \equiv \sqrt{\tau_w / \rho}$ denotes the wall friction velocity with the wall shear stress τ_w . The numbers of grids in three directions are $N_x = 384$, $N_y = 385$ and $N_z = 384$. The mesh sizes in wall units in the streamwise and spanwise directions are $\Delta x^+ = 3.04$ and $\Delta z^+ = 1.62$, respectively, and the distance of the first grid point from the wall is $\Delta y_w^+ = 0.00695$. Here, the superscript ‘+’ denotes a non-dimensional quantity scaled by the viscous length scale $\delta_\nu \equiv \nu / u_\tau$.

The computational domain of Eq. (9a) is selected as

$$\mathbf{x} \in [0, L_x] \times [0, L_y] \times [0, L_z/2], \quad (36)$$

where the symmetry of the velocity in the transitional channel flow is considered [29]. Since the vorticity is perpendicular to lateral boundaries at $z = 0$ and $z = L_z/2$ as $\omega_x|_{z=0, L_z/2} = \omega_y|_{z=0, L_z/2} = 0$, the Neumann boundary condition is used for ϕ_v at the lateral boundaries as

$$\left. \frac{\partial \phi_v}{\partial z}(\mathbf{x}, t; \tau) \right|_{z=0, L_z/2} = 0. \quad (37)$$

The Dirichlet boundary condition is used for ϕ_v at solid walls as

$$\begin{cases} \phi_v(\mathbf{x}, t; \tau)|_{y=0} = 0, \\ \phi_v(\mathbf{x}, t; \tau)|_{y=L_y} = L_y. \end{cases} \quad (38)$$

The periodic boundary condition is used for ϕ_v in the streamwise direction.

The initial VSF is determined as $\phi_0 = y$ by following the criteria proposed in [9]. The isosurfaces of ϕ_0 are parallel to the wall, and they are both stream surfaces and vortex surfaces, so they stay invariant in the laminar plane Poiseuille flow. The isosurfaces of ϕ_{v0} with $0 \leq \phi_{v0} \leq L_y/2$ represent the initial vortex surfaces from the bottom wall for $\phi_{v0} = 0$ to the mid-plane at $y = L_y/2$ for $\phi_{v0} = L_y/2$ within the lower half the channel.

The VSF scalar is calculated on the uniform grids $N_x \times N_y \times N_z = 768 \times 769 \times 768$ with ω interpolated onto the grids for the VSF calculation. The temporal evolution of isosurfaces of ϕ_v at different t in the transitional channel flow is shown in Fig. 6. The color on the isosurfaces of ϕ_v is rendered by $0 \leq |\omega| \leq 20$ from blue to red. Some vortex lines are integrated from the points on the extracted vortex surfaces.

As shown in Fig. 6, the temporal evolution of vortex surfaces can capture the reconnection of the hairpin-like vortical structures evolving from the initial planar surfaces in the transitional channel flow. In Figs. 6(a) and (b), the thumb-shaped bulge is lifted with the amplification of the initial disturbances. The edges of the bulge are rolled up into tube-like structures in Fig. 6(c), and the vortex tubes are stretched in Fig. 6(d). Subsequently, the vortex reconnection between the structures from opposite halves is observed in Figs. 6(e) and (f). This leads to scale cascade and further transition to turbulence. The evolution of the vortex surfaces calculated from the boundary-constraint method and the two-time method are very similar, which are further discussed in section 4.4. The comparison of the evolution of isosurfaces of the VSF and the Eulerian vortex criterion, and the effect of geometrical and topological changes of vortex surfaces on the drag generation in the laminar–turbulent transition are discussed extensively in [29].

4.3. Convergence of deviations in the VSF calculation

For the TG and transitional channel flows discussed in sections 4.1 and 4.2, the decay of the averaged deviation $\langle |\lambda_\omega| \rangle$ with pseudo-time τ is shown in Fig. 7. Since all the deviations are below 3%, the boundary-constraint method provides reasonable accurate VSF solutions in viscous flows.

The characteristic transfer time scale T_v defined in Eq. (29) can facilitate the estimation of the computational cost *a priori*. The parameters for calculating T_v are listed in Table 1 for the two flows. In numerical experiments, the half-value period

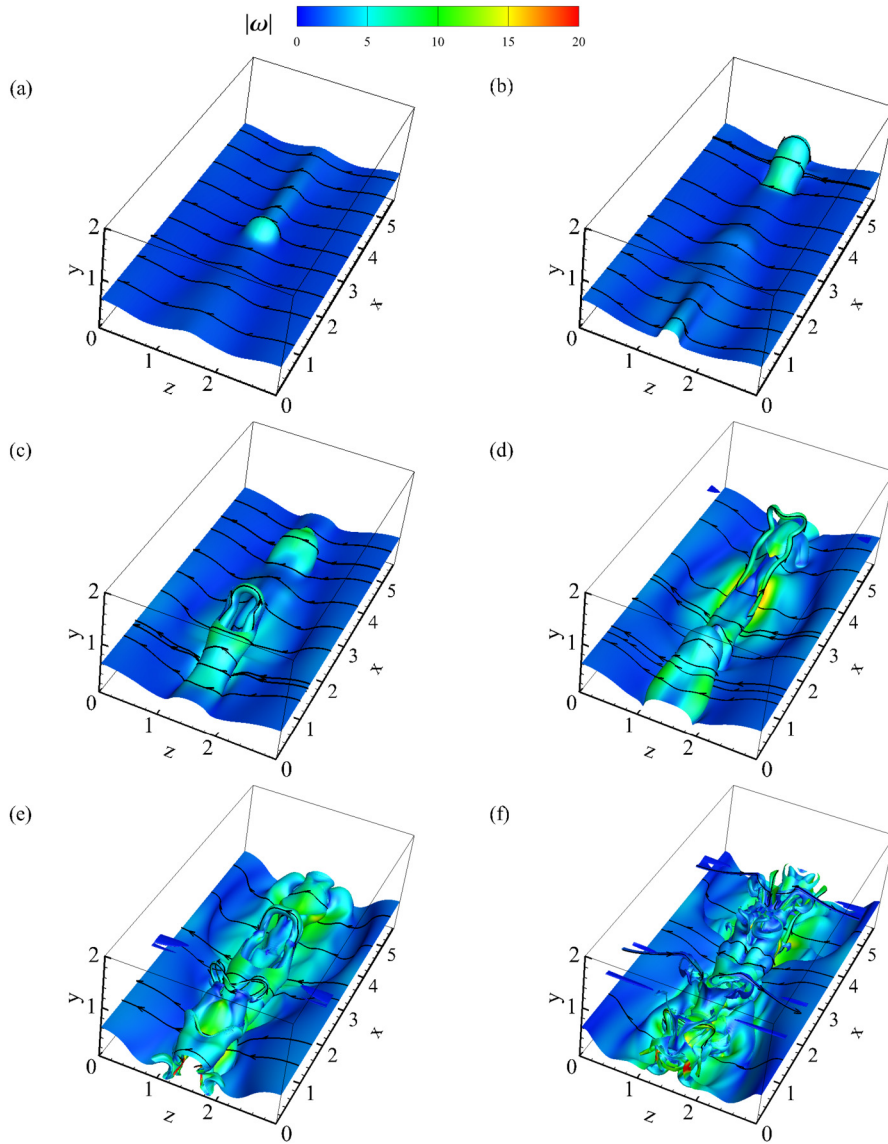


Fig. 6. Evolution of isosurfaces of the VSF in the transitional channel flow. Some vortex lines are integrated and plotted on the isosurfaces of $\phi_v = 0.6$. The color on the surfaces is rendered by $0 \leq |\omega| \leq 20$. (a) $t = 106$, (b) $t = 108$, (c) $t = 110$, (d) $t = 112$, (e) $t = 114$, (f) $t = 116$. (For interpretation of the colors in this figure, the reader is referred to the web version of this article.)

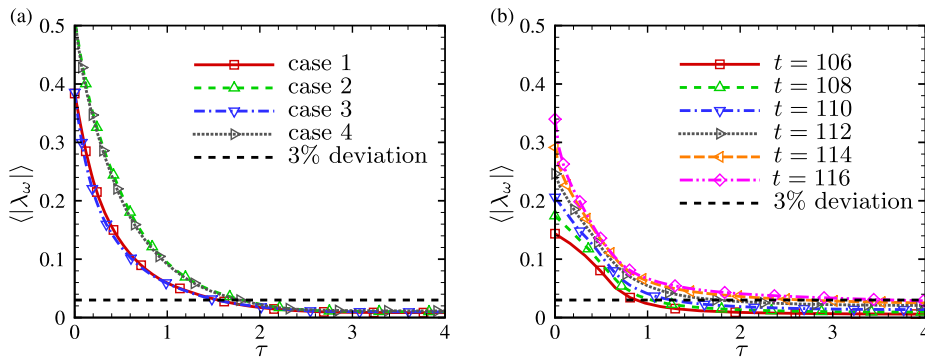


Fig. 7. Convergence of the averaged VSF deviation with increasing pseudo-time. (a) TG flow at $t = 6$ (case 1: $Re = 400$, $\phi_{v0} = \phi_{v0}^{(1)}$; case 2: $Re = 400$, $\phi_{v0} = \phi_{v0}^{(2)}$; case 3: $Re = 800$, $\phi_{v0} = \phi_{v0}^{(1)}$; case 4: $Re = 800$, $\phi_{v0} = \phi_{v0}^{(2)}$), (b) transitional channel flow at different times.

Table 1

Parameters for calculating the characteristic transfer time scale T_v in different cases. (a1) TG flow for $Re = 400$ and $\phi_{v0} = \phi_{v0}^{(1)}$, (a2) TG flow for $Re = 400$ and $\phi_{v0} = \phi_{v0}^{(2)}$, (a3) TG flow for $Re = 800$ and $\phi_{v0} = \phi_{v0}^{(1)}$, (a4) TG flow for $Re = 800$ and $\phi_{v0} = \phi_{v0}^{(2)}$, all the TG fields above are at $t = 6$; (b1) channel flow at $t = 106$, (b2) channel flow at $t = 108$, (b3) channel flow at $t = 110$, (b4) channel flow at $t = 112$, (b5) channel flow at $t = 114$, (b6) channel flow at $t = 116$.

Case	(a1)	(a2)	(a3)	(a4)	(b1)	(b2)	(b3)	(b4)	(b5)	(b6)
L_Ω	2.72	2.72	2.72	2.72	6.14	6.14	6.14	6.14	6.14	6.14
$\langle \omega \rangle$	1.48	1.48	1.74	1.74	2.16	2.25	2.39	2.60	2.91	3.23
$T_v = L_\Omega / \langle \omega \rangle$	1.84	1.84	1.56	1.56	2.84	2.73	2.57	2.36	2.11	1.90

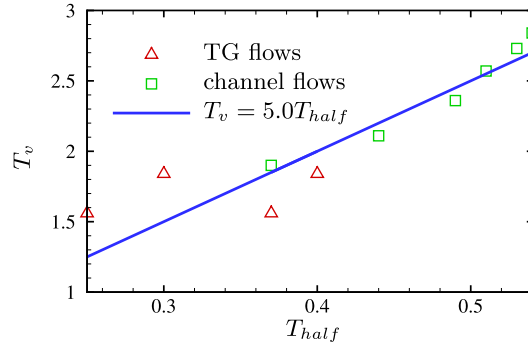


Fig. 8. Fitting of T_{half} from T_v . Triangles: from TG flows (Case a1–a4 in Table 1); squares: from channel flows (Case b1–b6 in Table 1); solid line: least-squares fit.

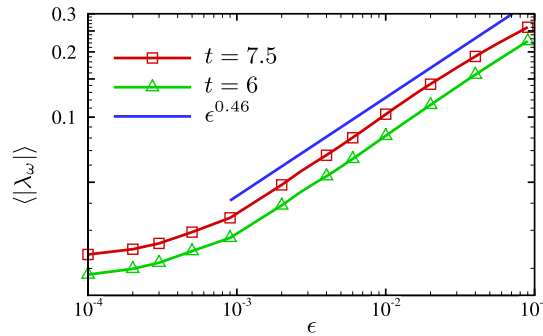


Fig. 9. Convergence of the averaged VSF deviation with different explicit diffusivities in the TG flow at $t = 6$ and $t = 7.5$ for $Re = 400$.

T_{half} of $\langle|\lambda_\omega|\rangle$ is introduced as a characteristic time scale for the decay of $\langle|\lambda_\omega|\rangle$, and we find that it can be approximated from T_v as a least-squares fit $T_v = 5.0T_{half}$. The correlation between T_{half} and T_v is shown in Fig. 8. Therefore, T_v is useful to estimate the order of the required total pseudo-time period T_τ for obtaining the VSF solution with the averaged deviation converged to a low level (e.g., less than 5%).

Besides T_τ , the effective diffusivity ϵ in Eq. (9a) is important on the numerical convergence of VSF solutions. In order to investigate the relation between $\langle|\lambda_\omega|\rangle$ and ϵ , we compute Eq. (9a) in TG flows with a range of explicit diffusivities from $\epsilon = 10^{-4}$ to 0.1 instead of the numerical diffusivity implicitly determined from the WENO scheme in former calculations. Here, the diffusion term in Eq. (9a) is approximated by the second-order central difference scheme. As the VSF solutions are converged for long pseudo-times, the plot of $\langle|\lambda_\omega|\rangle$ versus ϵ in the TG flow at $t = 6$ and $t = 7.5$ at $Re = 400$ is shown in Fig. 9. In Eq. (31), the growth of $\langle|\lambda_\omega|\rangle$ satisfies a power-law $f_\omega(\epsilon) = \epsilon^{0.46}$ at $0.001 < \epsilon < 0.1$. We remark that ϵ implicitly determined in the WENO scheme can be reduced by increasing grid resolution [31], so we can reach a compromise between the averaged deviation and the computational cost.

The CPU hours for constructing VSFs using the boundary-constraint method in the two flows are listed in Table 2. The CPU time depends on the desired deviation tolerance, the maximum value of the vorticity magnitude, and the complexity of the vortex lines in flow fields. We remark that the CPU hours for the boundary-constraint method are two orders of magnitude less than those for the two-time method in these cases with the same VSF deviation tolerance, and the boundary-constraint method only requires the DNS data at several physical times instead of a time series of DNS data which contain thousands of data files.

Table 2

CPU hours with three deviation tolerances in different cases. (a1) TG flow for $Re = 400$ and $\phi_{v0} = \phi_{v0}^{(1)}$, (a2) TG flow for $Re = 400$ and $\phi_{v0} = \phi_{v0}^{(2)}$, (a3) TG flow for $Re = 800$ and $\phi_{v0} = \phi_{v0}^{(1)}$, (a4) TG flow for $Re = 800$ and $\phi_{v0} = \phi_{v0}^{(2)}$, all the TG fields above are at $t = 6$; (b1) channel flow at $t = 106$, (b2) channel flow at $t = 108$, (b3) channel flow at $t = 110$, (b4) channel flow at $t = 112$, (b5) channel flow at $t = 114$, (b6) channel flow at $t = 116$.

$\langle \lambda_\omega \rangle$	Case									
	(a1)	(a2)	(a3)	(a4)	(b1)	(b2)	(b3)	(b4)	(b5)	(b6)
10%	0.3	0.4	0.5	0.7	87	99	226	450	509	573
5%	0.5	0.7	0.8	1.0	155	160	372	804	1139	1243
3%	0.7	0.8	1.1	1.3	206	221	538	1324	2405	3143

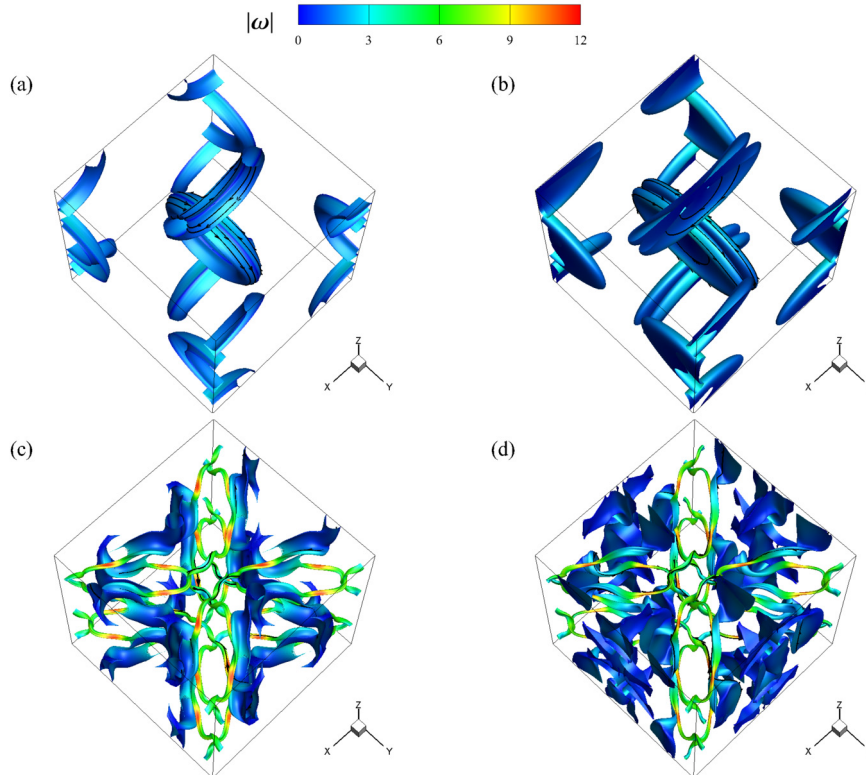


Fig. 10. Isosurfaces of the VSF calculated by two different methods in TG flows for $Re = 400$ (left column: the boundary-constraint method; right column: the two-time method). Color on the surfaces is rendered by $0 \leq |\omega| \leq 12$. Some vortex lines are integrated and plotted on the isosurfaces of ϕ_v . (a) and (b) $t = 3$, (c) and (d) $t = 7.5$. (For interpretation of the colors in this figure, the reader is referred to the web version of this article.)

4.4. Uniqueness of the VSF solution

Although the VSF constraint Eq. (1) can have multiple independent solutions [10,20], the two-time method appears to restore uniqueness to the indeterminate initial–boundary value problem [26,27]. Thus we should check the consistency of the boundary-constraint method and the two-time method, and investigate if the two methods can identify similar vortical structures.

The vortex surfaces in the TG flow for $Re = 400$ at different times using the two different VSF-construction methods are shown in Fig. 10. By comparing Figs. 10(a) and (b) in the transitional stage at $t = 3$, the topology of VSF isosurfaces from two methods shows differences on the connectivity of flattened vortex blobs [26]. On the other hand, by comparing Figs. 10(c) and (d) in the developed turbulent stage at $t = 7.5$, very similar coherent vortical structures are identified from the two methods. By cutting off the surfaces with small vorticity $|\omega| < 3$ that have minor influence on the flow dynamics, the strong, tube-like vortical structures constructed by the two different methods are almost identical in Fig. 11. The coherent vortex tubes appear to be an attractor in the chaotic vorticity system. The attractor is a bounded set of numerical values toward which a system tends to evolve, for a wide variety of initial conditions of the system [42,43]. Hence, the stable and robust geometry of vortex surfaces can be obtained from different VSF-construction methods in the flow with chaotic vortex lines.

For wall-bounded flows, the unique VSF solution can be obtained in the steady parallel shear flow with small disturbances under certain conditions, which is discussed in Appendix A. For general wall flows, two requirements on ϕ_v and

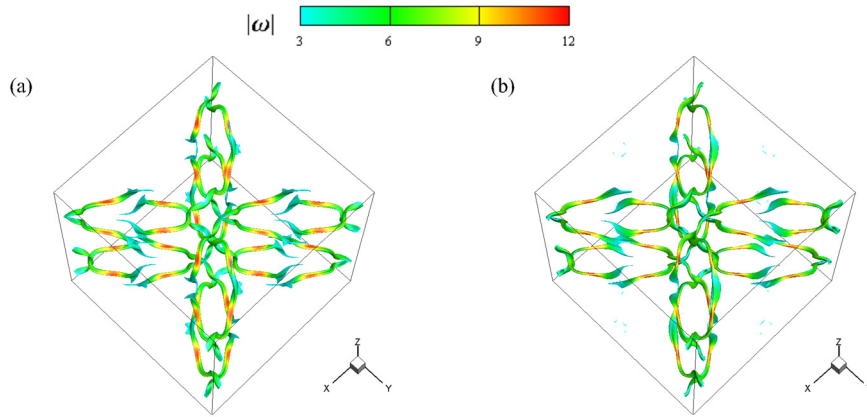


Fig. 11. Isosurfaces of the VSF with $|\omega| \geq 3$ extracted from the entire surfaces in Figs. 10(c) and (d). Color on the surfaces is rendered by $3 \leq |\omega| \leq 12$. (a) The boundary-constraint method, (b) the two-time method. (For interpretation of the colors in this figure, the reader is referred to the web version of this article.)

ω should be satisfied to obtain the unique VSF. First, we presume the spanwise vorticity ω_z is non-vanishing everywhere. Then the steady VSF solution of Eq. (1) is obtained from

$$\frac{\partial \phi_v}{\partial z} = -\frac{\omega_x}{\omega_z} \frac{\partial \phi_v}{\partial x} - \frac{\omega_y}{\omega_z} \frac{\partial \phi_v}{\partial y}. \quad (39)$$

According to the Cauchy–Kovalevskaya theorem [13], Eq. (39) has the unique solution for the given boundary condition ϕ_v at $z = 0$ or $z = L_z$. The second requirement is that ϕ_v at the lateral boundary remains unchanged in the VSF calculation from the two-time method and the boundary-constraint method. Thus, the steady VSF solution in the wall flow is determined by the initial ϕ_v at the lateral boundary, and the VSF can be kept consistent from the two methods. We remark that even the two requirements above are not strictly satisfied, we can still obtain nearly consistent VSFs from the two methods.

In our numerical experiment for transitional channel flow, first, the dominate shear motion results in strong ω_z . The spanwise vorticity is non-vanishing everywhere before vortex reconnection and can be zero at a finite number of locations during reconnection [29]. Second, the nearly laminar velocity–vorticity field at the lateral boundary is almost unaltered during the time period in the present study, and the initial VSF $\phi_v = y$ at the lateral boundary can stay invariant. Therefore, the two requirements of the unique VSF solution can be generally satisfied in our numerical experiment. We demonstrate that the evolution processes of vortex surfaces identified by the two methods are almost the same by comparing the results in [29] and in section 4.2.

In summary, VSF solutions for a specified vorticity field can be non-unique from different VSF-construction methods or initial conditions in the laminar or in the transitional stage unless some conditions depending on particular cases are satisfied. Nevertheless, relatively robust vortex surfaces in a developed turbulent flow can be obtained regardless of the construction method and initial condition.

5. Conclusions

In the present study, we develop the boundary-constraint method for constructing the VSF. For a given velocity–vorticity field at a specified time t , the numerical solution of the VSF is obtained by solving Eq. (9a). The initial condition Eq. (10) is a smooth scalar field that is compatible with the boundary condition Eq. (9b). In particular, the VSFs in TG flow and transitional channel flow are calculated by the boundary-constraint method.

The requirement of calculating VSFs by using the boundary-constraint method is that most of the vortex lines intersect boundaries of the computational domain. In the highly symmetric TG flow, although the vortex lines are closed, we cut the computational domain based on the symmetries of vorticity, and then calculate the VSF in a subdomain in which the vortex lines satisfy the requirement. In the transitional channel flow, the requirement of boundary-constraint method is satisfied owing to the dominating mean shear motion with vortex lines passing through lateral boundaries.

The comparison of the new boundary-constraint method and the existing two-time method [26] is summarized in Table 3. The boundary-constraint method is more feasible for constructing VSFs in complex shear flows than the two-time method. On the other hand, the two-time method is better for characterizing the continuous temporal evolution of vortical structures in the early transitional stage in a transitional flow. In the developed turbulent stage, the coherent tube-like vortical structures with strong vorticity extracted from these two different methods are almost identical. Therefore, the VSF is a good candidate to describe the evolution of vortical structures. In particular, the VSF evolution can be used to characterize stretching, rolling-up, twisting, and reconnection of vortex surfaces to elucidate the scale cascade in transitional flows [26,29].

Table 3
Comparison of the two methods for constructing the VSF.

	Boundary-constraint method	Two-time method
Velocity–vorticity dataset	Separate snapshots	Time-resolved series
Computational cost	Low	High
Requirement for the vorticity	Vortex lines passing boundaries	Vanishing helicity at t_0
Characterize time evolution	Conditional	Yes

The boundary-constraint method can be applied to construct other two-dimensional manifold of any smooth three-dimensional vector field. For example, we can construct the magnetic surface consisting of magnetic lines in magneto-hydrodynamic TG flows [44] using this method. Furthermore, the generalized, efficient VSF construction method should be developed for identifying unique evolving vortical structures in an arbitrary flow field.

Acknowledgements

The authors thank W. Su, Y. Zhao, J. Hao, and Q. Zhang for helpful comments. Numerical simulations were carried out on the TH-2A supercomputer in Guangzhou, China. This work has been supported in part by the National Natural Science Foundation of China (Grant Nos. 11472015, 11522215, 91541204, and 11521091), and the Thousand Young Talents Program of China.

Appendix A. Uniqueness of the VSF solution in simple shear flows

In this section, we discuss the uniqueness of the VSF solution in simple shear flows. The velocity field of a steady parallel shear flow is $\mathbf{u} = (U(y), 0, 0)$ where $U(y)$ is a smooth function, and the corresponding vorticity is $\boldsymbol{\omega} = (0, 0, -\partial U/\partial y)$. Substituting the vorticity into Eq. (1) yields the VSF equation $\partial\phi_v/\partial z = 0$. So the general VSF solution of the steady parallel shear flow can be expressed as $\phi_v = F(x, y)$, where F is an arbitrary continuously differentiable function.

Now we discuss the consistency of the boundary-constraint method and the two-time method in the steady parallel shear flow. The isosurface of $\phi_{v0} = \Phi(y)$ is selected as the streamwise–spanwise plane, where $\Phi(y)$ is an arbitrary smooth function. Since the isosurfaces of such initial condition stay invariant in the convection induced by vortex lines or stream lines, so the two methods construct the identical VSF. However, if the initial condition depends on x or z , the VSF isosurface can be stretched in different directions by the predictor Eq. (7) of the two-time method and the boundary-constraint equation (9a), so that the two methods construct different VSFs.

Next we consider the steady parallel shear flow with small disturbances. The velocity field is

$$\mathbf{u} = (U(y) + \epsilon_u(x, y, z), \epsilon_v(x, y, z), \epsilon_w(x, y, z)), \quad (\text{A.1})$$

where $\epsilon_i(x, y, z)$ with $i = u, v, w$ denotes a small disturbance. The corresponding vorticity is

$$\boldsymbol{\omega} = \left(\frac{\partial\epsilon_w}{\partial y} - \frac{\partial\epsilon_v}{\partial z}, \frac{\partial\epsilon_u}{\partial z} - \frac{\partial\epsilon_w}{\partial x}, -\frac{\partial U}{\partial y} + \frac{\partial\epsilon_v}{\partial x} - \frac{\partial\epsilon_u}{\partial y} \right). \quad (\text{A.2})$$

Since $\Phi(y)$ remains invariant in the calculation using two methods for the steady parallel shear flow, it is also used as the initial condition for constructing the VSF in the disturbed steady parallel shear flow. We set $\phi_v = \Phi(y) + \epsilon_\phi$ where ϵ_ϕ denotes the small variation of ϕ_v in the time or pseudo-time evolution. Then the predictor and the corrector of the two-time method can be respectively expressed as

$$\frac{\partial\epsilon_\phi}{\partial t} + (U + \epsilon_u) \frac{\partial\epsilon_\phi}{\partial x} + \epsilon_v \frac{\partial(\epsilon_\phi + \Phi)}{\partial y} + \epsilon_w \frac{\partial\epsilon_\phi}{\partial z} = 0, \quad (\text{A.3})$$

$$\frac{\partial\epsilon_\phi}{\partial \tau} + \left(\frac{\partial\epsilon_w}{\partial y} - \frac{\partial\epsilon_v}{\partial z} \right) \frac{\partial\epsilon_\phi}{\partial x} + \left(\frac{\partial\epsilon_u}{\partial z} - \frac{\partial\epsilon_w}{\partial x} \right) \frac{\partial(\epsilon_\phi + \Phi)}{\partial y} + \left(-\frac{\partial U}{\partial y} + \frac{\partial\epsilon_v}{\partial x} - \frac{\partial\epsilon_u}{\partial y} \right) \frac{\partial\epsilon_\phi}{\partial z} = 0. \quad (\text{A.4})$$

Ignoring the high order terms in Eqs. (A.3) and (A.4) yields

$$\frac{\partial\epsilon_\phi}{\partial t} + U \frac{\partial\epsilon_\phi}{\partial x} + \epsilon_v \frac{\partial\Phi}{\partial y} = 0, \quad (\text{A.5})$$

$$\frac{\partial\epsilon_\phi}{\partial \tau} + \left(\frac{\partial\epsilon_u}{\partial z} - \frac{\partial\epsilon_w}{\partial x} \right) \frac{\partial\Phi}{\partial y} - \frac{\partial U}{\partial y} \frac{\partial\epsilon_\phi}{\partial z} = 0. \quad (\text{A.6})$$

If $\epsilon_v = 0$ and $\partial\epsilon_\phi/\partial x = 0$, it is sufficient to obtain a steady solution of Eq. (A.5) in time. The vanishing $\partial\epsilon_\phi/\partial x$ requires that $\partial\epsilon_u/\partial z - \partial\epsilon_w/\partial x$ is independent of x in Eq. (A.6) with $\epsilon_\phi = 0$ in the initial condition. If the conditions above are satisfied, the predictor of the two-time method has no influence on the VSF calculation, then the two methods can construct the nearly identical VSF.

References

- [1] D. Küchemann, Report on the I.U.T.A.M. symposium on concentrated vortex motions in fluids, *J. Fluid Mech.* 21 (1965) 1–20.
- [2] J.C.R. Hunt, A. Wray, P. Moin, Eddies, stream, and convergence zones in turbulent flows, in: Center for Turbulence Research Report, Stanford, CA, USA, 1988, pp. 193–208.
- [3] J. Jeong, F. Hussain, On the identification of a vortex, *J. Fluid Mech.* 285 (1995) 69–94.
- [4] M.S. Chong, A.E. Perry, B.J. Cantwell, A general classification of three-dimensional flow field, *Phys. Fluids A* 2 (1990) 765–777.
- [5] J. Zhou, R.J. Adrian, S. Balachandar, T.M. Kendall, Mechanisms for generating coherent packets of hairpin vortices in channel flow, *J. Fluid Mech.* 387 (1999) 353–396.
- [6] J.Z. Wu, H.Y. Ma, M.D. Zhou, *Vorticity and Vortex Dynamics*, Springer, 2006.
- [7] P. Chakraborty, S. Balachandar, R.J. Adrian, On the relationships between local vortex identification schemes, *J. Fluid Mech.* 535 (2005) 189–214.
- [8] R. Cucitore, M. Quadrio, A. Baron, On the effectiveness and limitations of local criteria for the identification of a vortex, *Eur. J. Mech. B, Fluids* 18 (1999) 261–282.
- [9] Y. Zhao, Y. Yang, S. Chen, Evolution of material surfaces in the temporal transition in channel flow, *J. Fluid Mech.* 793 (2016) 840–876.
- [10] Y. Yang, D.I. Pullin, On Lagrangian and vortex-surface fields for flows with Taylor–Green and Kida–Pelz initial conditions, *J. Fluid Mech.* 661 (2010) 446–481.
- [11] G.K. Batchelor, *An Introduction to Fluid Dynamics*, Cambridge University Press, 1967.
- [12] P.G. Saffman, *Vortex Dynamics*, Cambridge University Press, 1992.
- [13] L.C. Evans, *Partial Differential Equations*, 2nd edition, American Mathematical Society, 2010.
- [14] L. Dieci, J. Lorenz, R.D. Russell, Numerical calculation of invariant tori, *SIAM J. Sci. Stat. Comput.* 12 (1991) 607–647.
- [15] L. Dieci, J. Lorenz, Block M-matrices and computation of invariant tori, *SIAM J. Sci. Stat. Comput.* 13 (1992) 885–903.
- [16] M. Huang, T. Kupper, N. Masbaum, Computation of invariant tori by the Fourier methods, *SIAM J. Sci. Comput.* 18 (1997) 918–942.
- [17] G. Haller, G. Yuan, Lagrangian coherent structures and mixing in two-dimensional turbulence, *Physica D* 147 (2010) 352–370.
- [18] G. Haller, Lagrangian coherent structures, *Annu. Rev. Fluid Mech.* 47 (2015) 137–162.
- [19] G. Haller, A. Hadjighasem, M. Farazmand, F. Huhn, Defining coherent vortices objectively from the vorticity, *J. Fluid Mech.* 795 (2016) 136–173.
- [20] P. He, Y. Yang, Construction of initial vortex-surface fields and Clebsch potentials for flows with high-symmetry using first integrals, *Phys. Fluids* 28 (2016) 037101.
- [21] H. Helmholtz, Über integrale der hydrodynamischen Gleichungen welche den Wirbelbewegungen entsprechen, *J. Reine Angew. Math.* 55 (1858) 25–55.
- [22] G.-H. Cottet, P. Koumoutsakos, *Vortex Methods: Theory and Practice*, Cambridge University Press, 2000.
- [23] P.S. Bernard, Vortex dynamics in transitional and turbulent boundary layers, *AIAA J.* 51 (2013) 1828–1842.
- [24] A.J. Chorin, P.S. Bernard, Discretization of a vortex sheet, with an example of roll-up, *J. Comput. Phys.* 13 (1973) 423–429.
- [25] K. Lindsay, R. Krasny, A particle method and adaptive treecode for vortex sheet motion in three-dimensional flow, *J. Comput. Phys.* 172 (2001) 879–907.
- [26] Y. Yang, D.I. Pullin, Evolution of vortex-surface fields in viscous Taylor–Green and Kida–Pelz flows, *J. Fluid Mech.* 685 (2011) 146–164.
- [27] D.I. Pullin, Y. Yang, Whither vortex tubes, *Fluid Dyn. Res.* 46 (2014) 061418.
- [28] S. Kida, M. Takaoka, Vortex reconnection, *Annu. Rev. Fluid Mech.* 26 (1994) 169–189.
- [29] Y. Zhao, Y. Yang, S. Chen, Vortex reconnection in the late transition in channel flow, *J. Fluid Mech.* 802 (2016) R4.
- [30] S. Gaudreault, J.A. Pudykiewicz, An efficient exponential time integration method for the numerical solution of the shallow water equations on the sphere, *J. Comput. Phys.* 322 (2016) 827–848.
- [31] G.S. Jiang, C.W. Shu, Efficient implementation of weighted ENO schemes, *J. Comput. Phys.* 126 (1996) 202–228.
- [32] J.Z. Wu, H.Y. Ma, M.D. Zhou, *Vortical Flows*, Springer, 2015.
- [33] C.C. Lalescu, B. Teaca, D. Carati, Implementation of high order spline interpolations for tracking test particles in discretized fields, *J. Comput. Phys.* 229 (2010) 5862–5869.
- [34] Q. Wang, Y.X. Ren, An accurate and robust finite volume scheme based on the spline interpolation for solving the Euler and Navier–Stokes equations on non-uniform curvilinear grids, *J. Comput. Phys.* 284 (2015) 648–667.
- [35] Y. Yang, D.I. Pullin, I. Bermejo-Moreno, Multi-scale geometric analysis of Lagrangian structures in isotropic turbulence, *J. Fluid Mech.* 654 (2010) 233–270.
- [36] G.I. Taylor, A.E. Green, Mechanism of the production of small eddies from large ones, *Proc. R. Soc. Lond. A* 158 (1937) 499–521.
- [37] M.E. Brachet, D.I. Meiron, S.A. Orszag, B.G. Nickel, R.H. Morf, U. Frisch, Small-scale structure of the Taylor–Green vortex, *J. Fluid Mech.* 130 (1983) 411–452.
- [38] Z.S. She, E. Jackson, S.A. Orszag, Intermittent vortex structures in homogeneous isotropic turbulence, *Nature* 344 (1990) 226–228.
- [39] J. Jimenez, A.A. Wray, P.G. Saffman, R.S. Rogallo, The structure of intense vorticity in isotropic turbulence, *J. Fluid Mech.* 255 (1993) 65–90.
- [40] J. Kim, P. Moin, R.D. Moser, Turbulent statistics in fully developed channel flow at low Reynolds number, *J. Fluid Mech.* 177 (1987) 133–166.
- [41] Y. Zhao, Z. Xia, Y. Shi, Z. Xiao, S. Chen, Constrained large-eddy simulation of laminar–turbulent transition in channel flow, *Phys. Fluids* 26 (2014) 095103.
- [42] E.N. Lorenz, Deterministic non-periodic flow, *J. Atmos. Sci.* 20 (1963) 130–141.
- [43] J. Milnor, On the concept of attractor, *Commun. Math. Phys.* 99 (1985) 177–195.
- [44] E. Lee, M.E. Brachet, A. Pouquet, P.D. Mininni, D. Rosenberg, Lack of universality in decaying magnetohydrodynamic turbulence, *Phys. Rev. E* 81 (2010) 016318.